Materials Science and Engineering B 287 (2023) 116106

Contents lists available at ScienceDirect

Materials Science & Engineering B

journal homepage: www.elsevier.com/locate/mseb

$Na_{0.67}Mn_{0.33}Ni_{0.33}Co_{0.33}O_2$: Effect of synthesis technique on competing P3 and P2 phases

S. Ecer [a], S. Altundağ [b], S. Altin [b], S. Avci [c,*]

[a] Nanoscience and Nanoengineering Program, Graduate School, Istanbul Medeniyet University, 34700 Istanbul, Türkiye
[b] Physics Department, Inonu University, 44280 Malatya, Türkiye
[c] Department of Engineering Physics, Istanbul Medeniyet University, 34700 Istanbul, Türkiye

ARTICLE INFO

Keywords:
Electrospin
Na-ion battery
$Na_{0.67}Mn_{0.33}Ni_{0.33}Co_{0.33}O_2$

ABSTRACT

In layered Na_xTMO_2 (TM = transition metal) common understanding attributes the emergence of *P*2 and *P*3 phases to the synthesis temperature. In this work, we show that the synthesis technique is the main responsible for these phases. We synthesize $Na_{0.67}Mn_{0.33}Ni_{0.33}Co_{0.33}O_2$ with two techniques, solid-state and electrospinning, using two temperatures, 700 °C and 900 °C. Both electrospun samples sintered at 900 °C and 700 °C show single phase *P*2 and *P*3, respectively. Both solid-state synthesized samples at 900 °C and 700 °C show mixture of *P*2/*P*3. Electrochemical properties of the sample with only *P*3 phase has the highest initial capacity of 130 $mAhg^{-1}$ at C/3 rate. The sample with only *P*2 phase has very stable cycle performance with 87 % capacity retention over 100 cycles consistent with its large interlayer separation. Our results show that the synthesis technique plays a crucial role in the crystal structure and the electrochemical performance of the layered cathode materials for Na-ion batteries.

1. Introduction

Na-ion batteries have been considered as an alternative for Li-ion batteries specifically for stationary and large-scale applications. Na owes this attention to its similar electrochemical properties with Li and natural abundance. The energy storage mechanism of Na-ion batteries is same as Li-ion counterparts except the larger size of Na^+ compared to Li^+ requires larger pathways to travel.

Layered Na_xTMO_2 (TM = transition metal) have been studied extensively since they provide large enough interlayer separation for Na ions to be inserted/extracted reversibly. These compounds are categorized into two main structures, *O*3 and *P*2 types. The labels indicate the Na coordination geometry and the number of repeat layers in the unit cell. In O3 type compounds, the x value in Na_xTMO_2 is close to 1 and the Na ions are accommodated in the octahedral sites. In *P*2 type, x is 2/3, and Na ions are accommodated in the prismatic sites [1]. 2 and 3 in *P*2 and *O*3 labels denote the number of edge-sharing TMO_6 octahedra with the oxygen stacking layers [2]. Less Na content in *P*2 type causes a smaller initial capacity than that of *O*3 type. However, due to open prismatic diffusion pathways, *P*2 type enables fast Na^+ diffusion and better cyclic performance [3]. Both of these compounds experience various phase transitions between O and P-type structures depending on the Na content during the charge and discharge process. These phase transitions are often responsible for poor cycling performance [1].

*P*3 structure with three-layered stacking is usually observed during the cycling of O3 type compounds and has been recently isolated by Ivanova *et al.* [4]. Crystal structures of *P*2 and *P*3-type Na_xTMO_2 are shown in Fig. 1. Na ions accommodate in the same prismatic sites in both *P*2 and *P*3-type compounds and *O*3 always transforms into *P*3 phase during the charge/discharge process. Therefore, *P*3 phase is connected to both *P*2 and *O*3 phases and expected to hold the positive effects of both phases [5]. In addition, *P*3-type Na deficient compounds can be used as cathode material for both Na- and Li-ion batteries [4,6].

The *P*3-type structure is obtained by sintering the compounds at lower temperatures than *P*2 equivalents. Guo *et al.* synthesized $Na_{0.67}Ti_{0.37}Cr_{0.63}O_2$ both in *P*2 and *P*3 phases via traditional solid state reaction after sintering at 1000 °C and 900 °C respectively [7]. Liu *et al.* used the gel combustion method to synthesize $Na_{0.5}Ni_{0.25}Mn_{0.75}O_2$ and obtained *P*3 and *P*2- type structures with annealing at 800 °C and 900 °C, respectively [8]. It is also possible to obtain biphasic compounds to observe the synergistic effects of both phases [9]. Kalapsazova *et al.* used a precursor-based method to synthesize $Na_{2/3}Ni_{1/3}Mn_{2/3}O_2$ with mixed *P*2/*P*3 phases after annealing at 700 °C and pure *P*2 phase after annealing at 900 °C [10]. Synergistic advantages of intergrowth mixed

* Corresponding author.
E-mail address: sevda.avci@medeniyet.edu.tr (S. Avci).

https://doi.org/10.1016/j.mseb.2022.116106
Received 5 January 2022; Received in revised form 1 September 2022; Accepted 28 October 2022
Available online 4 November 2022
0921-5107/© 2022 Elsevier B.V. All rights reserved.

phases in terms of electrochemical properties are observed in *P*2/*P*3 composite layered oxide compound ($Na_{0.5}Ni_{0.2}Co_{0.15}Mn_{0.65}O_2$) with synthesis temperature of 800 °C [9].

Both composition and the crystal structure of a cathode active material play very crucial role in the battery performance. However, the large radius of Na-ions requires suitable geometries to allow these ions to shuttle easily. One-dimensional nanostructures like nanofibers are particularly attractive due to their large surface area, short ion diffusion path and high deformation stress [11,12]. Electrospinning is a low-cost and large-scale technique to synthesize one-dimensional nanofiber with high porosity. So far there are few reports on layered Na-oxides synthesizes via electrospinning technique [13–15]. Desired crystal structures require high-temperature sintering of the as-spun nanofibers. However, high temperatures such as 700 °C or 900 °C usually deform the morphology of the as-spun nanofibers during crystallization [15–18].

In this work, we synthesized $Na_{0.76}Mn_{0.33}Ni_{0.33}Co_{0.33}O_2$ compound via electrospinning and conventional solid-state synthesis techniques (denoted as NF and SS, respectively). We applied two different sintering temperatures, 700 °C and 900 °C to observe the phase evaluation of *P*2 and *P*3 phases. We observe that both electrospun samples sintered at 700 °C (NF700) and 900 °C (NF900) show single phase *P*3 and *P*2 structures, respectively. However, both solid state synthesized samples sintered at 700 °C (SS700) and 900 °C (SS900) have mixture of *P*2 and *P*3 phases. Among the electrospun samples, 900 °C is high enough to destroy the nanofibers while at 700 °C nanofibers are able to survive partially. Electrochemical performances show that the highest initial discharge capacity of 130mAhg^{-1} (at C/3 rate) belongs to the NF700 sample (electrospun, sintered at 700 and has only *P*3 phase) along with the poorest cycle life with 54 % capacity retention (over 100 cyles at C/3 rate). On the other hand, NF900 sample (electrospun, sintered at 900 °C and has only *P*2 phase) has the highest capacity retention of 87 % (over 100 cyles at C/3 rate) owing to the stability of its structure. Our results clearly show that synthesis technique plays a crucial role in the final crystal structure and, as a consequence, the battery performance of the layered transition metal oxides for Na-ion batteries.

2. Materials and Methods

2.1. Solid-State synthesis

Metal oxides Na_2O_2, MnO_2, CoO_4, and NiO from Sigma Aldrich were mixed in stoichiometric amounts and ground with agate and mortar for one hour to prepare 4 g of the final composition. Half of the mixed powder was sintered at 700 °C and the other half at 900 °C with a heating rate of 5°/min. The samples stayed in the furnace for 24 h at the designated temperatures before they were quenched to room temperature.

2.2. Electrospinning technique

To prepare the electrospun nanofibers we followed the procedure explained in Ref [15]. Ethanol and 10 wt% polyvinylpyrrolidone (PVP, 1,300,000 g/mol) and N, *N*-dimethylformamide (DMF) were mixed and stirred with a magnetic stirrer to completely dissolve PVP. Then stoichiometric amounts of high purity sodium acetate, cobalt nitrate, manganese acetate, and nickel nitrate (all from Sigma Aldrich) were added to the solution. The solution was left for further stirring for overnight. During the stirring, the beaker was covered to prevent the evaporation of ethanol. The mixture was then transferred into a 21G syringe with a stainless steel needle. For the electrospinning process, the following parameters were used; the potential was 13.5 V, the distance between the needle and the Al foil collector was 14 cm and the feeding

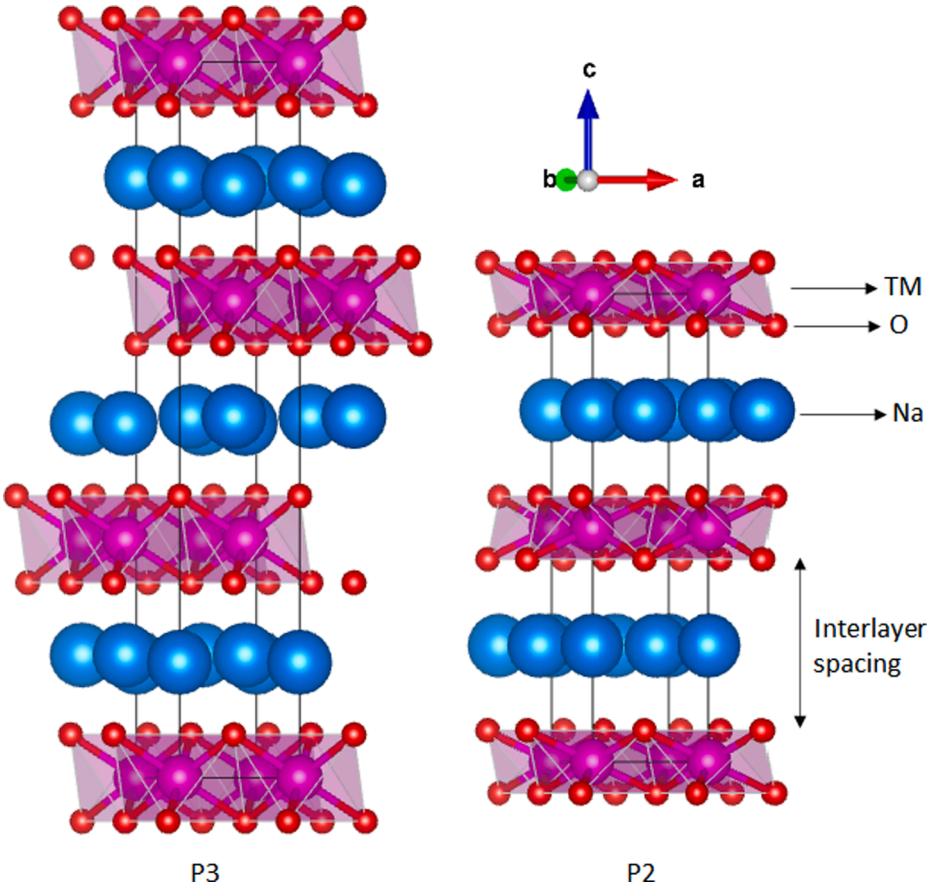


Fig. 1. Layered structures of *P*3 and *P*2 phases. Solid black lines represent the unit cells.

velocity was 0.7 ml/h. The nanofibers were deposited on Al foil however since the fibers stuck to the surface of the foil it was very hard to scratch the fibers from the surface of the foil and also a tiny amount of Al impurity was visible in the energy dispersive X-ray spectroscopy (EDS) analysis of our initial samples. Al doping has significant effects on electrochemical properties of layered transition metal oxide cathode materials for Na-ion batteries [19,20]. To eliminate the Al contamination and to make the collection process of the fibers easier, we used a special design of accordion shaped Al foil during the electrospinning process. The foil was folded into pleats with each crease was about 1 cm deep to form an accordion shape. Then the foil was mounted on a metal plate so that the distance between each pleat is about 1 cm wide. This way, the produced nanofibers form almost a self-standing layer on the accordion-shaped Al foil while only a small portion of them stuck to the pointy regions of the foil.

Then half of the collected fibers were sintered at 700 °C and the other half at 900 °C. Both samples were heated to the desired temperatures with a 1°/min heating rate and one-hour waiting time at every 100°C. The samples were kept at the final temperature for 12 h and then quenched to room temperature.

2.3. Structural characterization

Morphological characterizations and elemental analysis of the samples were performed via scanning electron microscope (SEM) and energy dispersive X-ray spectroscopy (EDS) by Thermo Scientific Quattro S at Science and Advanced Technologies Center at Istanbul Medeniyet University and Leo EVO-40 VPX SEM at Inonu University in Türkiye. The X-ray powder diffraction (XRD) patterns of the samples were obtained by Rigaku RadB Dmax diffractometer with CuKα (λKα = 1.5405 Å) radiation. GSAS-II open-source program [21] was used for Rietveld refinement [22] to analyze XRD data.

2.4. Electrochemical characterization

To fabricate CR2032 cells, the active material, super carbon and polyvinylidene fluoride (PVDF) (70 %: 15 %: 15 %) were mixed into slurries in *N*-methyl-2-pyrrolidone in an agate mortar and stirred with a magnetic stirrer for 24 h at room temperature. The mixture was coated onto aluminum foils by a micrometer adjustable film applicator blade then dried at 110 °C for 10 h under vacuum conditions. Discs (diameter 12 mm) of the coated films were punched and transferred to a glove box (Inert Technology, I-Lab) filled by spectroscopic argon gas. The amount of the active materials in the CR2032 cells was approximately 2.0 – 4.0 mg on the Al foil. CR2032 type coin cells with pure Na metal as the counter electrode were assembled in the glove box by using 1 M $NaClO_4$ in PC/EC ((1:1)v/v) electrolyte. Cyclic Voltammogram (CV) measurements were performed between 1.5 and 4.0 V at a scan rate of 0.1 mVs^{-1} bythe Ivium Octostat30. The Hefacycle BA100A battery analyzer was used for the galvanostatic charge/discharge measurements between 1.5 and 4.0 V at C/3 Ag^{-1} rate.

3. Results and discussion

3.1. Structure and morphology

In the Na_xTMO_2 family where TM is mixture of Mn/Ni/Co with various ratios have been studied previously. In this family of materials, Na stoichiometry results in O3-type layered structure [23]. In the Na deficient compositions, mostly Mn-rich ones have been studied such as $Na_{0.6}Mn_{0.65}Ni_{0.25}Co_{0.1}O_2$[24], $Na_{0.45}Ni_{0.22}Co_{0.11}Mn_{0.66}O_2$[25], $Na_{0.7}Mn_{0.6}Ni_{0.3}Co_{0.1}O_2$[26], $Na_{0.67}Ni_{0.167}Co_{0.167}Mn_{0.67}O_2$[27], etc. Most of these reports focus on the *P*2 structure which is obtained at high temperatures. Nguyen *et al.* studied the effect of calcination temperature on the structure of $Na_{0.6}Mn_{0.65}Ni_{0.25}Co_{0.1}O_2$ [24] via co-preticipation technique and report that 700 °C temperature treatment provides pure *P*3 structure while 800, 900, and 1000 °C yield pure *P*2 phase. Buchholz *et al.* obtained pure *P*2 phase after sintering at 800 °C in $Na_{0.45}Ni_{0.22}Co_{0.11}Mn_{0.66}O_2$ [25]. Yoshida *et al.* tested various ratios of Co/Mn/Ni to obtain pure *P*2 phase. They report that Mn-rich composition of $Na_{0.7}Mn_{0.6}Ni_{0.3}Co_{0.1}O_2$ yield pure *P*2 phase while the other compositions have NiO impurity after sintering at 900 °C [26]. To the best of our knowledge there are few studies reported on *P*2 or *P*3-type Na_xTMO_2 cathode material with Na deficiency and where TM = Mn/Co/Ni has a ratio of 1. In two of these reports, $Na_xCo_{1/3}Ni_{1/3}Mn_{1/3}O_2$ is synthesized via oxalate-acetate precursor method sintering at 800 °C yielding pure *P*3 type structure [2,4]. On the other hand, co-precipitation synthesis of $Na_{2/3}Ni_{1/3}Co_{1/3}Mn_{1/3}O_2$ combined with calcination at 850 °C yields *P*2 phase [19]. In another report, co-precipitation method combined with solid state synthesis is used to obtain *P*3-type $Na_{0.6}Co_{1/3}Ni_{1/3}Mn_{1/3}O_2$ after calcination at 350 °C for 36 h under pure oxygen flow [28].

In our study, we found that the synthesis method is the main cause regarding the structure of the yielded compounds. Fig. 2 shows the XRD data for our four samples. All our samples have less than 10 % NiO impurity. NF700 and NF900 show single phase *P*3 and *P*2 structures, respectively. This can be seen in the middle panel of Fig. 2. The absence of (10 $\bar{2}$) and (10 $\bar{5}$) reflections in the NF900 sample is clear evidence that NF900 sample does not contain *P*3 phase. In addition, the absence of (1 0 2) reflection in NF700 sample proves that *P*2 phase is not present in this sample.

We performed Rietveld refinement to calculate the cell parameters and interlayer spacings. We obtained good fit to the data when we used *P*63/*mmc* and *R*-3 m space groups for *P*2 and *P*3 phases, respectively. For SS900 and SS700 samples, we performed a two-phase refinement containing both *P*63/*mmc* and *R*-3 m symmetries. Rietveld refinements for SS900, SS700, NF900 and NF700 samples are shown in Fig. 3. Structural information, calculated cell parameters, phase fractions, and interlayer distances are listed in Table 1. There are some slight differences in the cell parameters for the same phases in the single phase samples and the biphasic samples. However, a significant difference between the c-axis of the *P*2 phase in the NF900 and the biphasic samples is conspicuous. This difference can also be seen in the right panel of Fig. 2. (0 0 2) peak for NF900 sample with pure *P*2 phase is clearly at different 2θ value than that of the other biphasic samples. Such difference in the c-axis of *P*2 phase between a sample with only *P*2 phase and a sample with multiphase where *P*2/O3 phases coexist was reported previously by Lee *et al.* They attribute this result to the higher sodium content in the multiphase sample due to presence of O3 phase leading to weaker repulsion of adjacent oxygen layers [29]. In our samples, *P*2 and *P*3 phases, weather they are single phase or coexist, contain same amount of Na content. Therefore above explanation cannot be valid for our samples. Smaller c-axis for the *P*2 phase of the biphasic samples can be attributed to the mismatch between the lattice parameters specifically c-axis of the *P*2 and *P*3 phases at the phase boundary that would result in microstrain [30].

Interlayer spacings are significantly different for different samples. Effects of both synthesis technique and sintering temperature on interlayer spacings are noticeable. In terms of the temperature, the interlayer distance for the samples sintered at 900 °C, are higher than the ones sintered at 700 °C for each synthesis technique. This can be explained by the larger strain in the samples caused by high sintering temperature [31,32]. In terms of synthesis techniques, interlayer separation is larger for electrospun samples than the solid state synthesized samples where the former ones are single phase while the latter ones are biphasic. As mentioned above, in the multiphase samples, c-axis difference between the two intergrown phases may cause microstrain in the phase boundaries causing smaller interlayer separation in these samples.

Above XRD results show that synthesis technique plays a crucial role in the emergence of *P*2 and *P*3 phases in layered Na metal oxides. We attribute these outcomes to the nature of the synthesis techniques that we used. In the solid-state synthesis technique as described in the

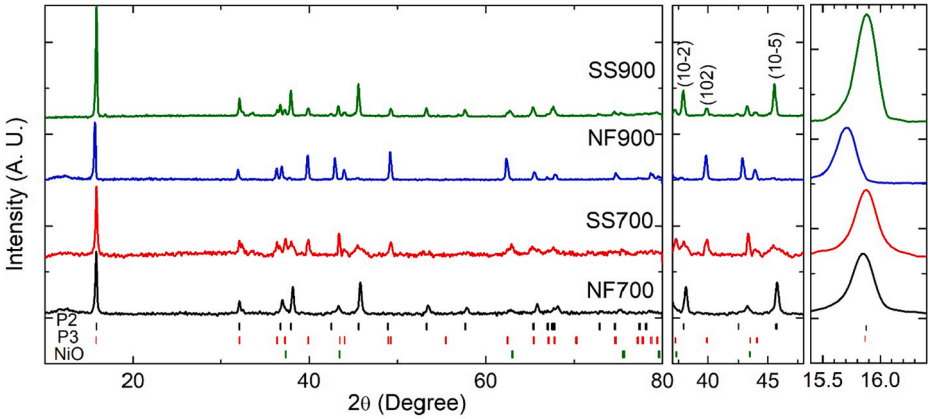


Fig. 2. XRD data for NF700, SS700, NF900, and SS900 samples. Green, red and black tick marks at the bottom of the Figure show the peak positions for NiO, *P*3 and *P*2 phases, respectively. The middle and the right panels show small ranges of the same data for easy comparison of the peaks. (For interpretation of the references to colour in this figure legend, the reader is referred to the web version of this article.)

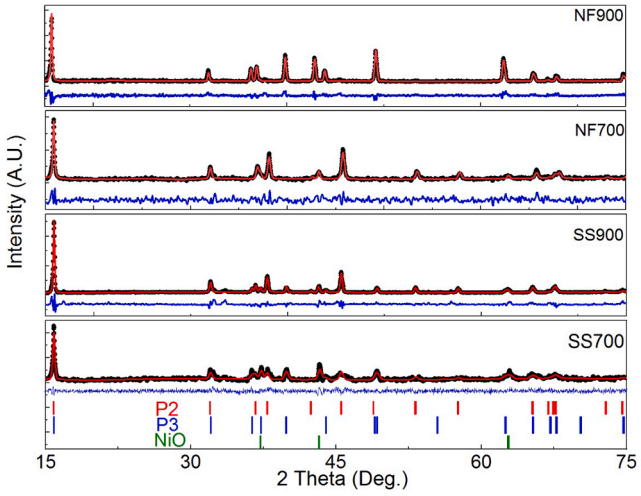


Fig. 3. Rietveld refinements of our four samples. R_{wp} and χ^2 values are listed in Table 1. Black dots, red solid, and blue solid lines represent the observed and calculated intensities and their differences, respectively. (For interpretation of the references to colour in this figure legend, the reader is referred to the web version of this article.)

Materials and Methods section that powders of metal oxides are used as the starting materials. The powders are mixed in an agate mortar and sintered at high temperatures to gain the desired crystal structures. The rate of the solid-state reaction greatly depends on the reaction conditions. It requires high temperatures since the reaction rate is limited by the slow diffusion of the solid phase, thus homogeneity of the mixture of the starting materials plays a crucial role [33]. In most cases, simple grinding the starting powders and using appropriate sintering temperatures yield well crystalline single-phase compounds in solid-state reaction technique. In our case, *P*3 is an intermediate metastable phase. Chagas *et al.* report that even slight changes in the sintering conditions including using different furnaces affect the proportions of *P*2 and *P*3 phases of biphasic compounds [34]. In other words, since the *P*3 phase is metastable, its emergence is very prone to the synthesis conditions. In this study, we used the same furnaces with the exact same heating and cooling protocols for all our samples. As opposed to solid state synthesis, in the electrospinning technique, the starting materials are mixed with the appropriate solvents to prepare a solution in a liquid state in which obtaining a homogenous solution via simple stirring is inevitable. The homogeneity is even taken forward through the electrospinning process which can be observed via SEM image of the as-spun fibers shown in Fig. 4(a). In short, the homogeneity of the mixture of the starting materials in electrospinning process due to its very nature facilitates the emergence of single phase *P*2 or *P*3 structures.

The thickness of the as-spun fibers in Fig. 4(a) is between 100 nm and 150 nm. These fibers are sintered at 700 °C (NF700) and 900 °C (NF900) for 12 h with a very slow heating rate and step-wise process as described in Ref [19], so the sample can retain its fibrous morphology. Although the fiber morphology is partially preserved at 700 °C (Fig. 4(b)), it is completely destroyed at 900 °C. The NF700 sample shows long 1D fibers with various thicknesses. 900 °C yields completely crystalline granular morphology for both NF900 (Fig. 4(c)) and SS900 (Fig. 4(e)) samples. In both samples, hexagonal crystals are noticeable confirming the crystal structures obtained from the XRD data. Fig. 4(f) shows the EDS data of the NF700 sample confirming the nominal composition of this sample. Kalluri *et al.* [15] report the partial preservation of the fiber morphology

Table 1
Structural parameters of NF700, NF900, SS700, and SS900 samples. Phase fractions are listed for P2 and P3 phases and the values are rounded for the sake of simplicity. All samples include less than 10 % NiO impurity.

Sample Name	Synthesis Method	Sintering Temp	Structure	Phase Fraction (*P*2/*P*3) %	a (Å)	c (Å)	Vol (Å^3)	Interlayer distance (*P*2/*P*3) (Å)	R_{wp} (%) /χ^2
NF700	Electrospun	700	*P*3	93(2)	2.8401(2)	16.7800(15)	117.219(16)	3.5238(67)	13.5/ 1.48
NF900	Electrospun	900	*P*2	92(1)	2.8521(4)	11.2620(18)	79.337(17)	3.5588(79)	8.5/1.2
SS700	Solid State	700	*P*2/*P*3 mixture	21(3)/71(2)	2.8563(6)/ 2.8574(19)	11.1691(19)/ 16.7740 (97)	78.917(30)/ 118.612(130)	3.4624(569)/ 3.4889 (570)	15.3/ 1.15
SS900	Solid State	900	*P*2/*P*3 mixture	34(1)/57(1)	2.8664(4)/ 2.8591(2)	11.1583(17)/ 16.7818(21)	78.845(17)/ 118.803(14)	3.4973(153)/ 3.4939 (69)	10.4/ 1.3

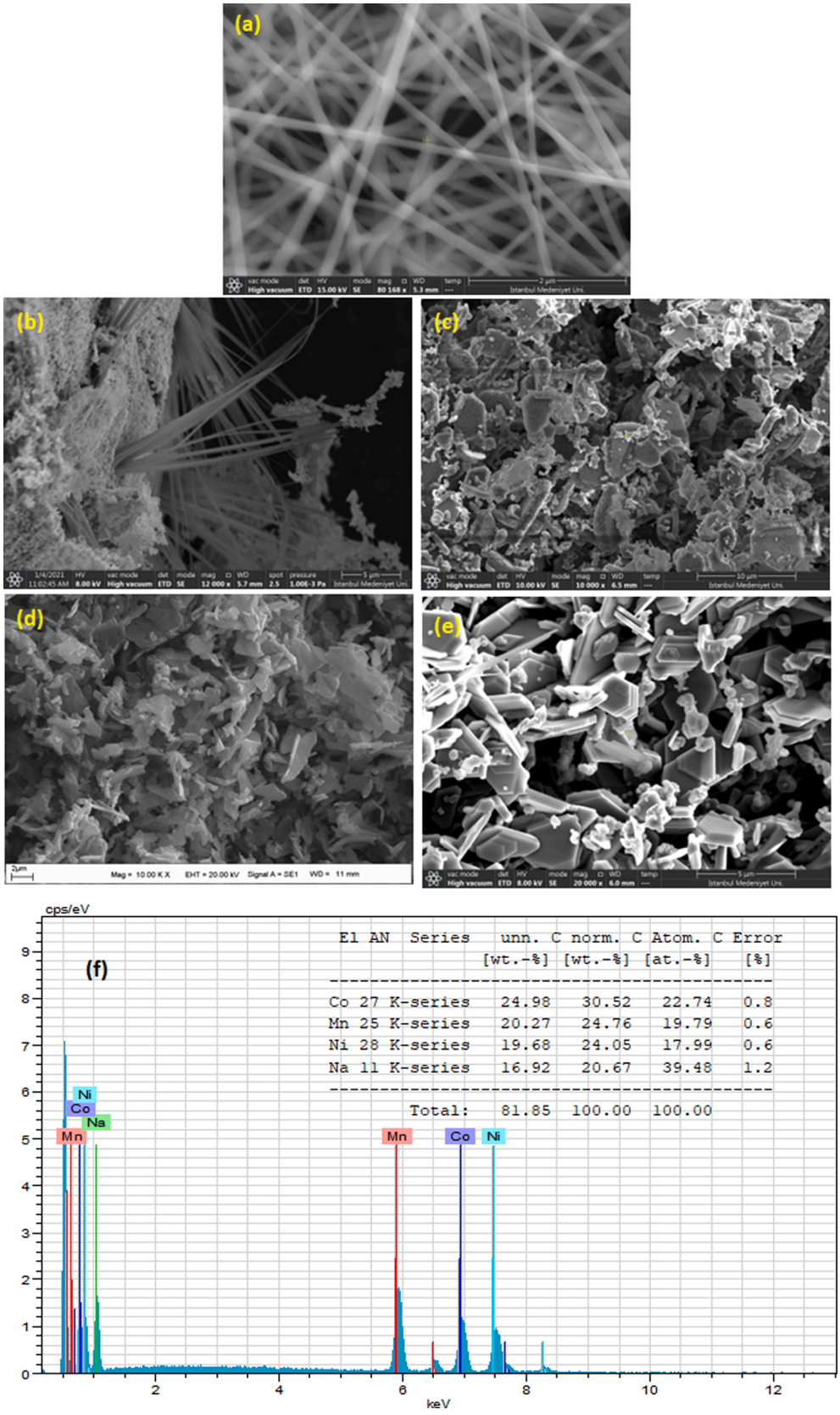


Fig. 4. SEM images of (a) Electrospun nanofibers before the heat treatment, (b) Electrospun nanofibers after sintering at 700 °C (NF700), (c) Electrospun sample after sintering at 900 °C (NF900). (d) Solid-state synthesis after sintering at 700 °C (SS700), (e) Solid-state synthesis after sintering at 900 °C (SS900), and (f) EDS analysis of NF700 sample. The data were collected from the region of this sample shown in (b) which includes both fibrous and granular morphology.

for *P*2-$Na_{2/3}Fe_{1/2}Mn_{1/2}O_2$ after a similar step-wise heating procedure up to 900 °C. Along with temperature and heating procedure, composition type may be effective in maintaining the fibers. We used the same solvents and polymer and same parameters for the electrospin process as described in the Kalluri *et al.*'s report [15], however the compositional differences may play a role in preserving the fiber morphology.

3.2. Electrochemical properties:

We performed cyclic voltammetry measurements on our samples at C/3 rate between 1.5 and 4.0 V, the data in Fig. 5 belong to the second cycles. In the voltammogram of both NF700 with pure *P*3 phase and NF900 with pure *P*2 phase, five anodic and corresponding cathodic peaks are observed. These peaks are 3.9/3.75, 3.48/3.43, 3.22/3.19, 2.32/1.97, and 2.01/1.83 V for NF700 sample and 3.92/3.89, 3.43/3.39, 3.17/3.12, 2.56/2.34, and 1.86/1.70 V for NF900 samples. Since SS700 and SS900 samples have multi-phase, their anodic and cathodic peaks are mixture of the voltammograms of *P*2 and *P*3 phases with several anodic and cathodic peaks. These peaks representing the multiple reversible phase transformations by Na/vacancy ordering in sodium layer or TMO_2 slabs in the transition-metal layer are consistent with the previous reports [35]. In our data, the complex shapes of the CV characteristics suggest that all $Ni^{2+}/Ni^{3+/4+}$, Co^{2+}/Co^{3+}, Co^{3+}/Co^{4+} and Mn^{3+}/Mn^{4+} redox pairs participate in the electrochemical reactions. For instance, the highest voltage peaks in both *P*3 and *P*2 phases around 3.9 V corresponds to the Ni^{2+}/Ni^{4+} redox couple as stated in Ref [36] and Ivanova *et al.* [4]. Zhu *et al.* [37] in *P*2-$Na_{0.67}Co_{0.5}Mn_{0.5}O_2$ and Yuan *et al.* [38] in *P*2-$Na_{0.67}[Mn_{0.65}Ni_{0.15}Co_{0.2}]O_2$ attributed the CV peaks around 3.5 V to Co^{3+}/Co^{4+} redox reactions. The CV peaks at 3.2 V is attributed to the Ni^{2+}/Ni^{3+} in *P*2-$Na_{2/3}Ni_{1/3}Mn_{2/3}O_2$. Mn^{3+}/Mn^{4+} redox couple is reported as being active below 3 V [37] and Co^{2+}/Co^{3+} is active below 2 V [39]. Thus, we attribute the two low redox peaks to Mn^{3+}/Mn^{4+} and Co^{2+}/Co^{3+}, respectively.

Fig. 6 compares the galvanostatic charge–discharge profiles of the four samples. The cells were tested between 1.5 and 4.0 V at C/3 current rate for 100 cycles. Several voltage plateaus are visible consistent with the redox peaks in CV data (Fig. 5). All of these charge–discharge profiles indicate that the phase transformations during the Na insertion/removal process are highly reversible.

Fig. 7 shows the cyclic performance of the four samples upon 100 cycles. NF700 sample with the pure *P*3 structure has roughly 30 % higher initial capacity of 130 $mAhg^{-1}$ at C/3 rate than the other three samples. We attribute such substantial difference to the partially preserved nano fiber morphology of the NF700 sample. As reported in earlier publications that nanofiber or nanowire type structure plays a crucial role in the Na-ion diffusion kinetics by forming a guided pathway for the charges [40]. However, this sample experiences a substantial capacity fade upon cycling. It loses almost half of its initial capacity with 100 cycles with a capacity retention of 54 %. Having low capacity retention is a characteristics of *P*3 phase as previously reported in Ref [41]. Guo *et al.* [7] compared the electrochemical performances of *P*2 and *P*3 structures on $Na_xTi_{0.37}Cr_{0.63}O_2$ compounds via experimental studies and density functional theory calculations. They stated that the Na diffusion barrier is less in *P*2 phase with smoother diffusion leading to better rate capability and cycling stability [7].

NF900 sample with pure *P*2 structure holds the best cycling performance among the four samples. Its capacity retention is 87 % over 100 cycles at C/3 rate. On the other hand, the biphasic SS700 and SS900 samples show similar cyclic behavior consistent with the XRD data. Their capacity retentions are 72 % for SS900 and 67 % for SS700. This slight difference can be attributed to the slightly higher *P*2 phase fraction of the SS900 sample (Table 1) with larger interlayer separation than the *P*2 phase in SS700 sample and lower diffusion barrier than the *P*3 phase. Chagas *et al.* [34] studied the effect of synthesis temperature on a similar composition, $Na_xNi_{0.22}Co_{0.11}Mn_{0.66}O_2$ synthesized via solid-state synthesis technique. In their work, they obtain pure *P*3 phase, a mixture of *P*3/*P*2 phases, and pure *P*2 phase by sintering at 700, 750, and 800 °C, respectively, with a phase fraction ratio of 70/30 for the biphasic sample. Our results for the biphasic compounds and the *P*2 phase are slightly better in terms of capacity retention due to the C-rate difference where they obtain 70 % and 87 % capacity retention for *P*3/*P*2 biphasic sample and pure *P*2 phase, respectively, over 100 cycles at 0.1C rate. We perfomed all our measurements in C/3 rate.

Due to sodium's large ionic radius, interlayer separation has

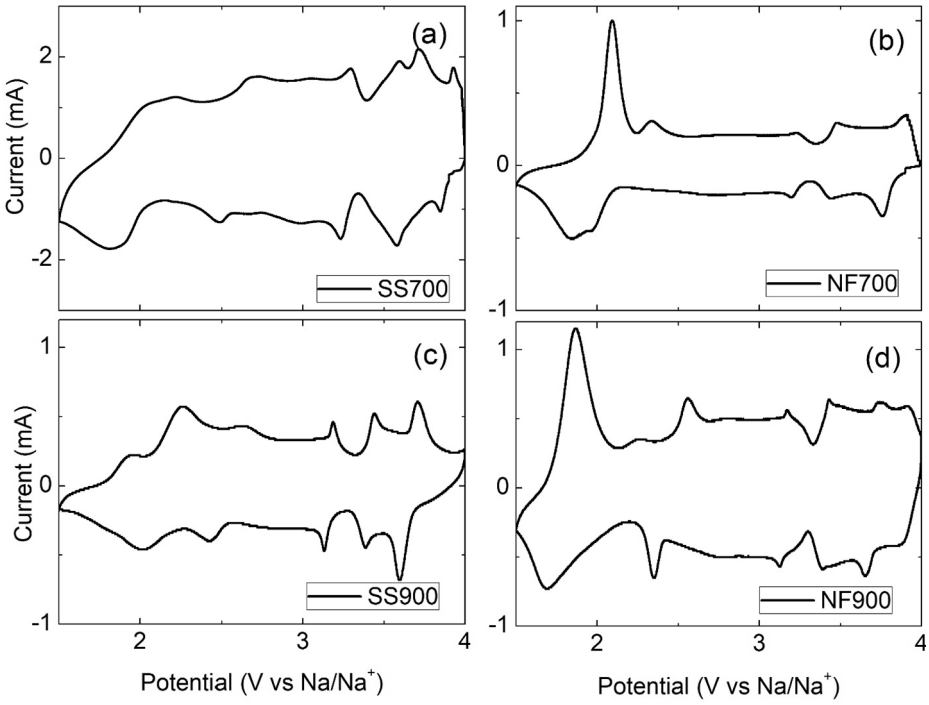


Fig. 5. Cyclic voltammetry data for a) SS700, b) NF700, c) SS900, d) NF900 at C/3 rate.

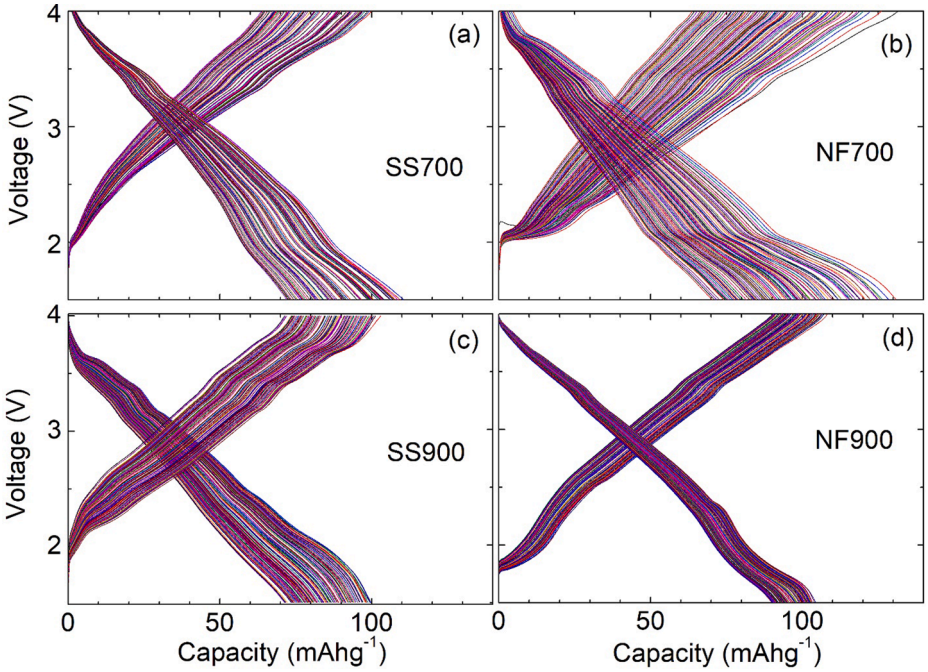


Fig. 6. Galvanostatic charge–discharge profiles of a) SS700, b)NF700, c) SS900, d)NF900 at C/3 rate.

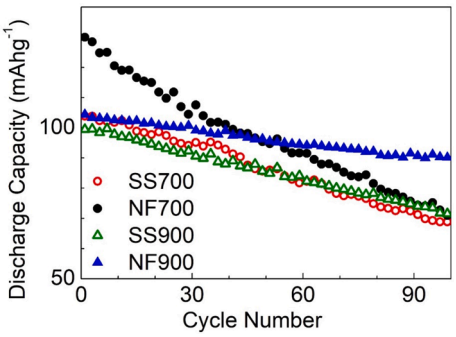


Fig. 7. The cyclic performance of the four samples with 100 cycles at C/3 rate.

substantial effects on the ion diffusion kinetics in Na_xTMO_2 family. Large interlayer spacing enhances the Na-ion mobility and leads to better electrochemical properties [41]. Larger interlayer spacings, listed in Table 1, for the electrospun samples are consistent with the electrochemical properties of the samples. NF900 sample with the best electrochemical performance among the four samples has the largest interlayer separation.

4. Conclusion

In this work, we studied the effects of the synthesis technique and the sintering temperature on the structure and electrochemical performance of $Na_{0.67}Mn_{0.33}Ni_{0.33}Co_{0.33}O_2$. We used two different synthesis techniques, i.e., solid-state synthesis and electrospinning, and two different sintering temperatures, i.e., 700 °C and 900 °C. We found that the synthesis technique plays a crucial role on the structure of the samples. We obtained pure *P*3 and pure *P*2 structures upon sintering the as-spun nanofibers at 700 °C and 900 °C, respectively. On the other hand, solid-state synthesis at 700 °C and 900 °C yielded biphasic samples containing both *P*3 and *P*2 phases. We attribute this result to the difference in the nature of the two synthesis techniques that electrospinning technique yield a superior homogeneity resulting in single-phase compounds. In terms of electrochemical performances, solid-state synthesized samples (SS700 and SS900) show very similar behavior due to similar crystal structures. On the other hand, electrospun samples sintered at 700 °C (NF700) and 900 °C (NF900) with pure *P*3 and *P*2 phases, respectively, show very distinct electrochemical behaviors. Among our samples, the NF900 sample shows the highest capacity retention (87 %) over 100 cycles with a relatively high initial capacity of 105 $mAhg^{-1}$ at C/3 rate. We attribute this result to the low diffusion barrier and large interlayer spacing of this sample.

Declaration of Competing Interest

The authors declare that they have no known competing financial interests or personal relationships that could have appeared to influence the work reported in this paper.

Data availability

Data will be made available on request.

Acknowledgement

S. Avci would like to acknowledge financial support of Istanbul Medeniyet University under project number F-GAP-2019-1498. S. Altin would like to acknowledge financial support of Inonu University under project number FBA-2019-1960. S. Avci would like to thank Prof. Murat Kazanci, Mr. Onur Aras and Mr. Enes Atas for their invaluable assistance in electrospinning experiments.

References

[1] C. Zhao, Z. Yao, Q. Wang, H. Li, J. Wang, M. Liu, S. Ganapathy, Y. Lu, J. Cabana, B. Li, X. Bai, A. Aspuru-Guzik, M. Wagemaker, L. Chen, Y.-S. Hu, Revealing High Na-Content P2-Type Layered Oxides as Advanced Sodium-Ion Cathodes, J. Am. Chem. Soc. 142 (2020) 5742–5750, https://doi.org/10.1021/JACS.9B13572.

[2] M. Kalapsazova, S. Ivanova, R. Kukeva, S. Simova, S. Wegner, E. Zhecheva, R. Stoyanova, Combined use of EPR and 23Na MAS NMR spectroscopy for assessing the properties of the mixed cobalt–nickel–manganese layers of P3-$Na_yCo_{1-2x}Ni_xMn_xO_2$, Phys. Chem. Chem. Phys. 19 (2017) 27065–27073, https://doi.org/10.1039/C7CP04849A.

[3] C. Ma, J. Alvarado, J. Xu, R.J. Clément, M. Kodur, W. Tong, C.P. Grey, Y.S. Meng, Exploring Oxygen Activity in the High Energy P2-Type $Na_{0.78}Ni_{0.23}Mn_{0.69}O_2$

Cathode Material for Na-Ion Batteries, J. Am. Chem. Soc. 139 (2017) 4835–4845, https://doi.org/10.1021/JACS.7B00164.
[4] S. Ivanova, E. Zhecheva, R. Kukeva, G. Tyuliev, D. Nihtianova, L. Mihailov, R. Stoyanova, Effect of Sodium Content on the Reversible Lithium Intercalation into Sodium-Deficient Cobalt–Nickel–Manganese Oxides $Na_xCo_{1/3}Ni_{1/3}Mn_{1/3}O_2$ ($0.38 \leq x \leq 0.75$) with a P3 Type of Structure, J. Phys. Chem. C. 120 (2016) 3654–3668, https://doi.org/10.1021/ACS.JPCC.5B11910.
[5] Y. Wang, X. Wang, X. Li, R. Yu, M. Chen, K. Tang, X. Zhang, The novel P3-type layered $Na_{0.65}Mn_{0.75}Ni_{0.25}O_2$ oxides doped by non-metallic elements for high performance sodium-ion batteries, Chem. Eng. J. 360 (2019) 139–147, https://doi.org/10.1016/J.CEJ.2018.11.214.
[6] M. Kalapsazova, R. Stoyanova, E. Zhecheva, G. Tyuliev, D. Nihtianova, Sodium deficient nickel–manganese oxides as intercalation electrodes in lithium ion batteries, J. Mater. Chem. A. 2 (2014) 19383–19395, https://doi.org/10.1039/C4TA04094E.
[7] S. Guo, Y. Sun, J. Yi, K. Zhu, P. Liu, Y. Zhu, G.Z. Zhu, M. Chen, M. Ishida, H. Zhou, Understanding sodium-ion diffusion in layered P2 and P3 oxides via experiments and first-principles calculations: A bridge between crystal structure and electrochemical performance, NPG Asia Mater. 8 (2016). https://doi.org/10.1038/am.2016.53.
[8] J. Liu, C. Didier, M. Sale, N. Sharma, Z. Guo, V.K. Peterson, C.D. Ling, Elucidation of the high-voltage phase in the layered sodium ion battery cathode material P3–$Na_{0.5}Ni_{0.25}Mn_{0.75}O_2$, J. Mater. Chem. A. 8 (2020) 21151–21162, https://doi.org/10.1039/D0TA06600A.
[9] P. Hou, J. Yin, X. Lu, J. Li, Y. Zhao, X. Xu, A stable layered P3/P2 and spinel intergrowth nanocomposite as a long-life and high-rate cathode for sodium-ion batteries, Nanoscale. 10 (2018) 6671–6677, https://doi.org/10.1039/C8NR00650D.
[10] M. Kalapsazova, G.F. Ortiz, J.L. Tirado, O. Dolotko, E. Zhecheva, D. Nihtianova, L. Mihaylov, R. Stoyanova, P3-Type Layered Sodium-Deficient Nickel-Manganese Oxides:AFlexible Structural, Matrix for Reversible Sodium and Lithium Intercalation 80 (11) (2015) 1642–1656.
[11] C. Li, M. Qiu, R. Li, X. Li, M. Wang, J. He, G. Lin, L. Xiao, Q. Qian, Q. Chen, J. Wu, X. Li, Y.-W. Mai, Y. Chen, Electrospinning Engineering Enables High-Performance Sodium-Ion Batteries, Adv. Fiber Mater. 4 (2022) 43–65, https://doi.org/10.1007/S42765-021-00088-6/FIGURES/8.
[12] S. Peng, P.R. Ilango, Electrospinning of Nanofibers for Na-Ion Battery, Electrospinning Nanofibers Batter, Appl. (2020) 61–83, https://doi.org/10.1007/978-981-15-1428-9_3.
[13] H. Li, Y. Bai, F. Wu, Y. Li, C. Wu, Budding willow branches shaped $Na_3V_2(PO_4)_3$/C nanofibers synthesized via an electrospinning technique and used as cathode material for sodium ion batteries, J. Power Sources. 273 (2015) 784–792, https://doi.org/10.1016/J.JPOWSOUR.2014.09.153.
[14] M. Guan, J. Chen, X. Zhang, L. Yang, B. Wang, S. Zhong, Yarn-ball-shaped P2-$Na_{2/3}Fe_{1/2}Mn_{1/2}O_2$ nanofibers prepared by magnetic-assisted electrospinning method as high-performance cathode material for Na-ion batteries, Mater. Lett. 254 (2019) 24–27, https://doi.org/10.1016/J.MATLET.2019.07.001.
[15] S. Kalluri, K. Hau Seng, W. Kong Pang, Z. Guo, Z. Chen, H.K. Liu, S.X. Dou, Electrospun P2-type $Na_{2/3}(Fe_{1/2}Mn_{1/2})$ O_2 hierarchical nanofibers as cathode material for sodium-ion batteries, ACS Appl. Mater. Interfaces. 6 (2014) 8953–8958, https://doi.org/10.1021/AM502343S/SUPPL_FILE/AM502343S_SI_001.PDF.
[16] Y. Hu, L. Wu, G. Liao, Y. Yang, F. Ye, J. Chen, X. Zhu, S. Zhong, Electrospinning synthesis of Na_2MnPO_4F/C nanofibers as a high voltage cathode material for Na-ion batteries, Ceram. Int. 44 (2018) 17577–17584, https://doi.org/10.1016/J.CERAMINT.2018.06.236.
[17] X. Ding, H. Zhou, G. Liu, Z. Yin, Y. Jiang, X. Wang, Electrochemical evaluation of $LiAl_{0.05}Ni_{0.05}Mn_{1.9}O_4$ cathode material synthesized via electrospinning method, J. Alloys Compd. 632 (2015) 147–151, https://doi.org/10.1016/J.JALLCOM.2015.01.163.
[18] B. Fu, X. Zhou, Y. Wang, High-rate performance electrospun $Na_{0.44}MnO_2$ nanofibers as cathode material for sodium-ion batteries, J. Power Sources. 310 (2016) 102–108, https://doi.org/10.1016/J.JPOWSOUR.2016.01.101.
[19] J. Fu, H. Huang, K. Shi, F. Chen, Z. Yang, W. Zhang, Al-doped walnut-shell-like P2-type $Na_{2/3}Ni_{1/3}Co_{(1/3-x)}Mn_{1/3}Al_xO_2$ as advanced sodium ion battery cathode materials with enhanced rate and cycling performance, Electrochim. Acta. 349 (2020), 136347, https://doi.org/10.1016/J.ELECTACTA.2020.136347.
[20] A. Ma, Z. Yin, J. Wang, Z. Wang, H. Guo, G. Yan, Al-doped $NaNi_{1/3}Mn_{1/3}Fe_{1/3}O_2$ for high performance of sodium ion batteries, Ionics (Kiel). 26 (2020) 1797–1804, https://doi.org/10.1007/S11581-019-03437-Z/FIGURES/7.
[21] B.H. Toby, R.B. Von Dreele, GSAS-II: The genesis of a modern open-source all purpose crystallography software package, J. Appl. Crystallogr. 46 (2) (2013) 544–549.
[22] H.M. Rietveld, A profile refinement method for nuclear and magnetic structures, J. Appl. Crystallogr. 2 (1969) 65–71, https://doi.org/10.1107/s0021889869006558.
[23] M. Sathiya, K. Hemalatha, K. Ramesha, J.-M. Tarascon, A.S. Prakash, Synthesis, Structure, and Electrochemical Properties of the Layered Sodium Insertion Cathode Material: $NaNi_{1/3}Mn_{1/3}Co_{1/3}O_2$, Chem. Mater. 24 (2012) 1846–1853, https://doi.org/10.1021/CM300466B.
[24] N.-A. Nguyen, K. Kim, K.H. Choi, H. Jeon, K. Lee, M.-H. Ryou, Y.M. Lee, Effect of Calcination Temperature on a P-type $Na_{0.6}Mn_{0.65}Ni_{0.25}Co_{0.10}O_2$ Cathode Material for Sodium-Ion Batteries, J. Electrochem. Soc. 164 (2016) A6308, https://doi.org/10.1149/2.0511701JES.
[25] D. Buchholz, A. Moretti, R. Kloepsch, S. Nowak, V. Siozios, M. Winter, S. Passerini, Toward Na-ion Batteries—Synthesis and Characterization of a Novel High Capacity Na Ion Intercalation Material, Chem. Mater. 25 (2013) 142–148, https://doi.org/10.1021/cm3029615.
[26] J. Yoshida, E. Guerin, M. Arnault, C. Constantin, B.M. de Boisse, D. Carlier, M. Guignard, C. Delmas, New P2 - $Na_{0.70}Mn_{0.60}Ni_{0.30}Co_{0.10}O_2$ Layered Oxide as Electrode Material for Na-Ion Batteries, J. Electrochem. Soc. 161 (2014) A1987, https://doi.org/10.1149/2.0121414JES.
[27] S. Bao, S.-H. Luo, Z.-Y. Wang, S.-X. Yan, Q. Wang, J.-y. Li, Novel P2-type concentration-gradient $Na_{0.67}Ni_{0.167}Co_{0.167}Mn_{0.67}O_2$ modified by Mn-rich surface as cathode material for sodium ion batteries, J. Power Sources. 396 (2018) 404–411.
[28] M. Matsui, F. Mizukoshi, H. Hasegawa, N. Imanishi, Ca-substituted P3-type $Na_xNi_{1/3}Mn_{1/3}Co_{1/3}O_2$ as a potential high voltage cathode active material for sodium-ion batteries, J. Power Sources. 485 (2021), 229346, https://doi.org/10.1016/J.JPOWSOUR.2020.229346.
[29] E. Lee, J. Lu, Y. Ren, X. Luo, X. Zhang, J. Wen, D. Miller, A. DeWahl, S. Hackney, B. Key, D. Kim, M.D. Slater, C.S. Johnson, Layered P2/O3 Intergrowth Cathode: Toward High Power Na-Ion Batteries, Adv. Energy Mater. 4 (2014) 1400458, https://doi.org/10.1002/AENM.201400458.
[30] E. Gabriel, D. Hou, E. Lee, H. Xiong, Multiphase layered transition metal oxide positive electrodes for sodium ion batteries, Energy Sci. Eng. 10 (2022) 1672–1705, https://doi.org/10.1002/ESE3.1128.
[31] P. Mishra, Sonia, P. Kumar, Kumar, Effect of sintering temperature on dielectric, piezoelectric and ferroelectric properties of BZT–BCT 50/50 ceramics, J. Alloys Compd. 545 (2012) 210–215.
[32] A. Ullah, C.W. Ahn, A. Hussain, I.W. Kim, The effects of sintering temperatures on dielectric, ferroelectric and electric field-induced strain of lead-free $Bi_{0.5}(Na_{0.78}K_{0.22})_{0.5}TiO_3$ piezoelectric ceramics synthesized by the sol–gel technique, Curr. Appl. Phys. 10 (2010) 1367–1371, https://doi.org/10.1016/J.CAP.2010.05.004.
[33] C. Ando, H. Chazono, H. Kishi, Effect of Particle Size and Mixing Homogeneity of Starting Powder on Solid State Synthesis of BaTiO3 3 (2004), https://doi.org/10.4028/www.scientific.net/KEM.269.161.
[34] L.G. Chagas, D. Buchholz, C. Vaalma, L. Wuab, S. Passerini, P-type $Na_xNi_{0.22}Co_{0.11}Mn_{0.66}O_2$ materials: linking synthesis with structure and electrochemical performance, J. Mater. Chem. A. 2 (2014) 20263–20270, https://doi.org/10.1039/C4TA03946G.
[35] D.D. Yuan, Y.X. Wang, Y.L. Cao, X.P. Ai, H.X. Yang, Improved electrochemical performance of Fe-substituted $NaNi_{0.5}Mn_{0.5}O_2$ cathode materials for sodium-ion batteries, ACS Appl. Mater. Interfaces. 7 (2015) 8585–8591, https://doi.org/10.1021/ACSAMI.5B00594/ASSET/IMAGES/MEDIUM/AM-2015-00594V_0009.GIF.
[36] Y. Li, J. Liu, Y. Lei, C. Lai, Q. Xu, Enhanced electrochemical performances of Na-doped cathode material $LiNi_{1/3}Co_{1/3}Mn_{1/3}O_2$ for lithium-ion batteries, J Mater Sci 52 (23) (2017) 13596–13605.
[37] Y.E. Zhu, X. Qi, X. Chen, X. Zhou, X. Zhang, J. Wei, Y. Hu, Z. Zhou, A P2-$Na_{0.67}Co_{0.5}Mn_{0.5}O_2$ cathode material with excellent rate capability and cycling stability for sodium ion batteries, J. Mater. Chem. A. 4 (2016) 11103–11109, https://doi.org/10.1039/C6TA02845D.
[38] D. Yuan, W. He, F. Pei, F. Wu, Y. Wu, J. Qian, Y. Cao, X. Ai, H. Yang, Synthesis and electrochemical behaviors of layered $Na_{0.67}[Mn_{0.65}Co_{0.2}Ni_{0.15}]O_2$ microflakes as a stable cathode material for sodium-ion batteries, J. Mater. Chem. A. 1 (2013) 3895–3899, https://doi.org/10.1039/C3TA01430D.
[39] Q.-C. Wang, E. Hu, Y. Pan, N. Xiao, F. Hong, Z.-W. Fu, X.-J. Wu, S.-M. Bak, X.-Q. Yang, Y.-N. Zhou, Q.-C. Wang, Y. Pan, N. Xiao, F.X. Hong, J. Wu, Y.-N. Zhou, E. Hu, S.-M. Bak, X.-Q. Yang, Z.-w., Fu, Utilizing Co2+/Co3+ Redox Couple in P2-Layered $Na_{0.66}Co_{0.22}Mn_{0.44}Ti_{0.34}O_2$ Cathode for Sodium-Ion Batteries, Adv. Sci. 4 (2017) 1700219, https://doi.org/10.1002/ADVS.201700219.
[40] D. Kong, Y.e. Wang, S. Huang, Y.V. Lim, J. Zhang, L. Sun, B.o. Liu, T. Chen, P. Valdivia y Alvarado, H.Y. Yang, Surface modification of $Na_2Ti_3O_7$ nanofibre arrays using N-doped graphene quantum dots as advanced anodes for sodium-ion batteries with ultra-stable and high-rate capability, J. Mater. Chem. A. 7 (20) (2019) 12751–12762.
[41] D. Tie, G. Gao, F. Xia, R. Yue, Q. Wang, R. Qi, B. Wang, Y. Zhao, Modulating the Interlayer Spacing and Na + /Vacancy Disordering of P2-$Na_{0.67}MnO_2$ for Fast Diffusion and High-Rate Sodium Storage, ACS Appl. Mater. Interfaces. 11 (2019) 6978–6985, https://doi.org/10.1021/ACSAMI.8B19134/SUPPL_FILE/AM8B19134_SI_001.PDF.